Annales Geophysicae (2005) 23: 221–230
SRef-ID: 1432-0576/ag/2005-23-221

Annales Geophysicae

An imaging interferometry capability for the EISCAT Svalbard Radar

T. Grydeland[1], **J. L. Chau**[2], **C. La Hoz**[3,1], **and A. Brekke**[1]

[1]Dept. of Physics, University of Tromsø, N-9037 Tromsø, Norway
[2]Radio Observatorio de Jicamarca, Instituto Geofísico del Perù, Perù
[3]currently at: Cornell University, Earth and Atmospheric Science Department, Ithaca, NY 14853, USA

Received: 14 October 2003 – Revised: 2 July 2004 – Accepted: 20 August 2004 – Published: 31 January 2005

Part of Special Issue "Eleventh International EISCAT Workshop"

Abstract. Interferometric imaging (aperture synthesis imaging) is a technique used by radio astronomers to achieve angular resolution that far surpasses what is possible with a single large aperture. A similar technique has been used for radar imaging studies of equatorial ionospheric phenomena at the Jicamarca Radio Observatory. We present plans for adding an interferometric imaging capability to the EISCAT Svalbard Radar (ESR), a capability which will contribute significantly to several areas of active research, including naturally and artificially enhanced ion-acoustic echoes and their detailed relation in space and time to optical phenomena, polar mesospheric summer echoes (PMSE), and meteor studies.

Interferometry using the two antennas of the ESR has demonstrated the existence of extremely narrow, field-aligned scattering structures, but having only a single baseline is a severe limitation for such studies. Building additional IS-class antennas at the ESR is not a trivial task. However, the very high scattering levels in enhanced ion-acoustic echoes and PMSE means that a passive receiver antenna of more modest gain should still be capable of detecting these echoes.

In this paper we present simulations of what an imaging interferometer will be capable of observing for different antenna configurations and brightness distributions, under ideal conditions, using two different image inversion algorithms. We also discuss different antenna and receiver technologies.

Key words. Ionosphere (instruments and techniques) – Radio science (interferometry) – Space plasma physics (instruments and techniques)

Correspondence to: T. Grydeland
(tom.grydeland@phys.uit.no)

1 Interferometric imaging

In radio astronomy, angular resolutions are regularly obtained which far surpass those of the individual antennas. Several relatively small aperture elements are used with coherent detectors by employing an interferometric imaging technique (aperture synthesis imaging) (e.g. Taylor et al., 1999). The interferometric technique is different from, and in some sense complementary to, the technique of phased array beam steering (cf. Röttger and Ierkic, 1985).

Incoherent scattering (IS) is usually a volume scattering process, where interferometry can contribute little. There are exceptions, however. When the scattering angle is very close to perpendicular with the magnetic field, the scattered spectrum changes rapidly with aspect angle, and this was used by Woodman (1971) to make very accurate measurements of the direction of the equatorial magnetic field using a single interferometric baseline.

In the equatorial electrojet (EEJ), scattering is often very strong and from localized regions, and Farley et al. (1981) extended the radar interferometry technique to measure the full complex cross-spectrum (where phase is an indication of position) and used the technique to measure the drift velocity of scattering irregularities in the electrojet.

A radar with multiple receiving antennas can use interferometry with multiple baselines to construct true images of the radar targets illuminated by the transmitting antenna beam. It is well known that interferometry using a single antenna baseline yields two moments of the radio brightness distribution, the distribution of received power versus bearing (Farley et al., 1981). Interferometry with multiple baselines yields multiple moments, and the totality of these moments can be inverted to reconstruct the brightness distribution versus azimuth and zenith angle. The inversion essentially amounts to performing a Fourier transform of the interferometry cross-spectra (Briggs et al., 1999). However, since the cross-spectra are inevitably sampled incompletely due to

the limited number of interferometry baselines available, and because of the presence of statistical fluctuations in the data, the inversion should be performed using statistical inverse methods to achieve satisfactory results (Ables, 1974; Jaynes, 1982).

The first examples of ionospheric radar interferometric observations interpreted in terms of images were provided by Kudeki and Sürücü (1991), using four receiving antennas with nonredundant spacing, resulting in six baselines. For imaging of the scattering from equatorial spread-F, Hysell (1996) introduced the Maximum Entropy algorithm pioneered for applications in radio astronomy (Wilczek and Drapatz, 1985). This is considered a "superresolution" method, since the resolution of the images it produces is not limited by the Nyquist sampling theorem. Our problem differs from the one in radio astronomy mainly in that radar range gating adds the third dimension to the images. In addition, the time evolution of the scattering medium in the radar case can be evaluated by comparing images from successive data integrations. A comprehensive review of radar imaging was made by Woodman (1997).

Since the pioneering work of Kudeki and Sürücü (1991) to study the EEJ, radar imaging has been improved and extended to study other phenomena. At Jicamarca, these include equatorial spread-F (Hysell, 1999), lower atmosphere and meteors (Chau and Woodman, 2001, 2004), while mid-latitude E-region irregularities are beginning to be studied using radar imaging at the Piura and MU radars. There are also plans to add imaging capabilities to the SuperDARN station on Kodiak Island in Alaska to study the auroral electrojet irregularities (D. L. Hysell, private communication).

2 Scientific objectives

2.1 Naturally enhanced ion-acoustic echoes

At high latitudes, very enhanced ion-acoustic echoes are often seen in connection with precipitation (aurora) (Collis et al., 1991; Sedgemore-Schulthess et al., 1999). These echoes have recently been identified with dynamic rayed aurora (Blixt et al., 2005), and the enhancement has been shown to arise in very localized filaments using radar interferometry with a single baseline (Grydeland et al., 2003).

Temporal correlations have been found between radar scattering intensity and optical intensity, (Grydeland et al., 2004), but the detailed spatial relation between auroral forms and radar scattering structures can only be studied when the full horizontal distribution of the scattering is known, using radar imaging.

If these enhanced echoes are in fact associated with auroral structures, then we would expect the spatial structure of these echoes to match the fine structure of the aurora. On the other hand, one might expect that enhancement in the two ion-acoustic shoulders of the IS spectra could arise in physically separate regions, for instance, in adjacent upward and return regions of field-aligned currents.

Although Grydeland et al. (2003, 2004) show evidence of both ion-acoustic shoulders being enhanced simultaneously and in the same volume, an appeal to statistical arguments is necessary to resolve the ambiguity resulting from the single-baseline interferometric technique. Multiple baselines and unambiguous imaging would conclusively decide this issue, in addition to allowing for detailed study of the spatial and temporal correlation between the intensification in the optical aurora and localized radar backscatter.

Although this is our primary objective for the construction of passive receiving antennas for interferometry, we can also imagine a number of other applications, once such a capability has been established.

2.2 Heating-enhanced echoes

Under construction in the immediate vicinity of the ESR is an HF heating facility called Space Plasma Exploration by Active Radar, or SPEAR (Wright et al., 2000). Heating experiments at Arecibo and in Tromsø have revealed spatial structures on many different spatial scales. The rocket observations reported by Kelley et al. (1995) show 10-m density depletions (filaments, or ducts) collected into "bunches" on spatial scales of 60 to 600 m, which again make up "patches" of sizes between 1.5 and 6 km. An imaging interferometry setup like the one discussed here should be able to detect the bunches on the intermediate scale. The filaments themselves are not likely to be resolved without longer baselines than those discussed here, while the patches are as large as or larger than the radar beam and are better studied using beam-swinging techniques. At the same time, artificial heating has been associated with optical emissions, with a strong aspect angle dependence (Isham et al., 1999; Kosch et al., 2000; Rietveld et al., 2003, and references therein). Combining an imaging radar with high-resolution optical instruments can prove to be very interesting.

This application adds technical challenges. As the properties in the scattering medium is highly stratified near the HF matching height, very good range resolution is required. Therefore, phase coding techniques must be used, which may not work as well for interferometry as the plain pulses used previously.

Even so, we expect that a radar imaging capability will be an important and attractive addition to such observations, in the same way that it contributes to naturally enhanced scattering. Detailed correlations in time and space between the heater beam, optical emissions and enhanced radar scattering will be available for study for the first time.

2.3 PMSE observations

Observations have been made of Polar Mesospheric Summer Echoes (PMSE) at the ESR (Hall and Röttger, 2001), and from this and observations at other observatories (cf. Cho and Röttger, 1997, and references therein), we know that the scattering layer is very thin and often subdivided into several scattering layers, not necessarily having the same properties.

Radar imaging of PMSE at 52 MHz was recently demonstrated by Yu et al. (2001), who concluded that horizontal structure was involved when the Doppler frequency of the PMSE region underwent sudden transitions. From coordinated PMSE observations using the colocated SOUSY Svalbard Radar at 53.5 MHz and the ESR at 500 MHz (Röttger, 2000), we know that there is a large difference in the scattering between these frequency regions, and we expect an imaging capability to be an important addition to the study of the high-latitude mesosphere.

2.4 Meteor studies

Characterization of meteor head and trail echoes are very important for a number of studies, for example, radiant, trajectories, velocity and acceleration calculations, which in turn translate to accurate measurements of meteor mass, etc. Observations of meteor heads are very demanding, however, and only recent advances in technology have allowed most of the large-aperture high-power radar systems to start contributing to the understanding of these echoes. Observations have been made at EISCAT (Pellinen-Wannberg and Wannberg, 1994), Arecibo (Zhou and Kelley, 1997), Millstone Hill (Erickson et al., 2001), ALTAIR (Close et al., 2002), etc. However, most of these observations are limited to line-of-sight, which means that they are not able to characterise the meteor in 3-D. Exceptional are the reported observations of meteors with the tristatic EISCAT UHF radar system (Janches et al., 2002).

Chau and Woodman (2004) used the Jicamarca radar in an interferometric imaging mode to determine where in the sky meteors are coming from. A somewhat surprising result is that even during the Leonid meteor shower, the overwhelming majority of the meteors seen by the radar are clustered around the apex, the point in the sky that the Earth is headed towards at any given time, and Sulzer (2004), using the Arecibo radar, has been able to corroborate the Jicamarca findings for the majority of meteors they have observed at different seasons.

Observations of a similar nature at the ESR have the potential to provide a 3-D capability without a full tristatic radar system. Such a capability would have the advantage over the Jicamarca system of a high-latitude position, which means that meteors in the ecliptic plane coming from directions other than the apex would be less shielded by the Earth. We therefore expect an imaging capability at the ESR to provide important additions to our knowledge of the meteor population of our solar system.

3 Technology considerations

Once the scientific applications for an imaging capability have been described, it is useful to see what technological requirements these applications lead to. Two fundamental quantities are involved: scattering strength, which dictates the antenna and receiver gain and noise figure required to obtain a useful SNR, and the expected size and distribution of scatterers, which dictates the number of receiving antennas and their spatial distribution. Representative scattering strengths and angular sizes for the various phenomena are summarized in Table 1.

Table 1. A summary of the properties of the various physical phenomena expected to be observed with the ESR imaging interferometer. The SNRs have been taken from examples used in the references, and represent strong, but not atypical cases. Since some of these phenomena have not yet been observed with the ESR at all, the SNR has been interpolated or extrapolated from observations at other frequencies. The sizes are not listed for meteor trails, as these can have a number of different orientations (from horizontal to vertical) and will gradually expand in size from the initial radius of a few centimetres to a few tens of metres, to where it has been dissolved into the background.

	SNR	Altitude	Horiz. size	Angle
Nat. enh. echoes	20 dB	500 km	500 m	0.05°
HF-enh. echoes	25 dB	150 km	600 m	0.23°
PMSE	6 dB	85 km	3 km	2°
Meteor heads	15 dB	100 km	2 cm	10^{-5}°
Meteor trails	30 dB	100 km	*	*

Since the primary objective is imaging of naturally enhanced ion-acoustic echoes, the requirements are stated in relation to this objective. How well the other objectives are served will be discussed at the end of this section.

3.1 Antenna alternatives

Total scattering levels from enhanced ion-acoustic echoes can be anywhere between barely exceeding the thermal level up to as much as 50 dB above this level at high altitudes (Ogawa et al., submitted, 2003[1]). As this figure was obtained from a 10 s integration, while Grydeland et al. (2003) have shown that the dynamics of such enhancements occur on time scales closer to 0.2 s, the instantaneous enhancement in strong events might be even higher. Such strong events are relatively rare, however.

The ESR, using the steerable 32 m antenna, has a system temperature of approximately 70 K and a gain of 42.5 dBi. With this antenna used to transmit and receive, Grydeland et al. (2003) observed SNR of 20 dB at altitudes of 500 km for 0.2 s integrations during an enhancement event much less spectacular than those reported by Ogawa et al. (submitted, 2003)[1].

3.1.1 Parabolic dish antennas

At first, one might imagine that smaller parabolic dishes are the obvious choice for receiving antennas. As it turns

[1]Ogawa, Y., Buchert, S. C., Fujii, R., Nozawa, S., and Forme, F.: Naturally enhanced ion-acoustic lines at high altitudes, Ann. Geophys., submitted, 2003.

out, such dishes do not scale very well to smaller antennas. The wavelength of the signal remains the same (60 cm for the ESR), and the dish geometry becomes less favourable as the antenna decreases in size. A useful rule of thumb is that the main reflecting surface should be no less than $50\,\lambda$ in diameter (G. Wannberg, private communication), which corresponds to 30 m at 500 MHz, only marginally smaller than the existing steerable antenna. Erecting such an antenna is a project of greater scope than intended for our purpose.

A Cassegrain (two-reflector) design makes the problems worse, since the sub-reflector (secondary reflecting surface) becomes proportionally larger as the main reflector shrinks. Smaller Cassegrain dishes also have increasingly severe problems with spillover from the subreflector, beyond the edges of the main surface, resulting in noise from the ground being received, as well as problems arising from refraction around the edges of the sub-reflector and its supports.

Even though a primary focus feed might alleviate some of the problems described above, parabolic dishes of a size suitable for this purpose turn out to be prohibitively expensive compared to the other antenna alternatives described below.

3.1.2 Panel antennas

Panel antennas are commonly used for radio and television transmission. These antennas have good uniform gain patterns, are often made for combination into arrays, and they can be made to cover broad frequency bands. They turn out to be less than perfectly suited for our application, however, as they are oriented more towards broad uniform coverage than to forming narrow beams.

3.1.3 Yagi arrays

Better results are expected from using an array of Yagi elements for the passive antennas. A frequency of 500 MHz corresponds to band 24 of commercial UHF television transmission, so there are good antennas commercially available. Such antennas can be combined into arrays with a minimum of engineering. In addition to the much lower cost, such a solution also has the attractive property of minimal environmental impact. Such an array would be supported on the ground at a small number of points, and tied down by guy wires. Otherwise, it does not obstruct air flow, precipitation or even sunlight from reaching the vegetation below.

One commercially available antenna is an 18-element Yagi with a reported gain of 15.5 dB, optimized for UHF bands 24 and 25. This antenna is 2676 mm long, and weighs 0.9 kg. If we conservatively assume a gain increase of 2.5 dB for every doubling of the array size, we can achieve a total gain of 25.5 dB using a 4×4 array. With a spacing of 2λ, or 1.2 m, between the antennas, such an array would take up about $4\,\mathrm{m}\times4\,\mathrm{m}$. Since the array will be pointed close to vertical, and will not have to be steered, the assembly, mounting and pointing of the antennas in a frame are expected to be quite straightforward.

A disadvantage with this solution is that the ESR uses circular polarization, while the Yagi is sensitive to one linear polarization, which results in a 3 dB loss in sensitivity. We have not been able to find a commercial supplier of long Yagis of crossed dipoles, but they should be possible to make if the extra gain proves to be necessary.

3.2 Analog/digital receiver

Since the signal received in the passive antennas is to be correlated with the signal in the existing ESR antennas, it is important that all signals are kept phase coherent. It would therefore be an advantage if the analog part of the receiver were to mirror that of the ESR to a large degree.

To shield the receiver, intended to receive the weak signal from the ionosphere, from being overwhelmed by the transmit power from the active antennas, a receiver protector synchronized with the ESR radar controllers must be included. This will add to the noise figure of the array. Since the array will be placed in the near field of both the large antennas, the actual power levels to be inhibited by this receiver protector must be determined through accurate measurements on the exact sites of the array.

The analog part of the receiver will be built to resemble the one used in the existing ESR receiver (Wannberg et al., 1997), and synchronised with this through the site frequency reference. For the initial deployment of a single antenna, the signal will be routed through the old ESR analog/digital receiver chain, which is currently used as a plasma line receiver. For the full deployment, the digitization and processing of the received signal will be made through a multi-channel MIDAS-W type receiver (Holt et al., 2000; Grydeland et al., 2005) using software from the Open Radar Initiative (Lind et al., 2003).

3.3 Imaging techniques

Using the terminology of Woodman (1997), the visibility function $\boldsymbol{v}$ measurable on the ground and the brightness distribution $\boldsymbol{B}$ in the scattering volume are related through a discrete Fourier Transform. The purpose of the imaging algorithm is to obtain an estimate of the brightness distribution, an image, from the sparsely sampled estimate of the visibility function. Chau and Woodman (2001) described and compared four different image inversion techniques. In the present work, we will only consider two of these, the Maximum Entropy method (Jaynes, 1982; Hysell, 1996, 1999) and the Capon algorithm (Capon, 1969), as these seem to perform better than other methods for a variety of model (true) images.

Previously employed (Fourier-based) imaging algorithms take whatever data are available and construct an image from these data, modifying the technique if necessary (for example, by applying windowing functions, pre-whitening, etc.) to avoid spurious features, or possibly removing features from the constructed image, as in the CLEAN algorithm well known from radio astronomy (Högbom, 1974).

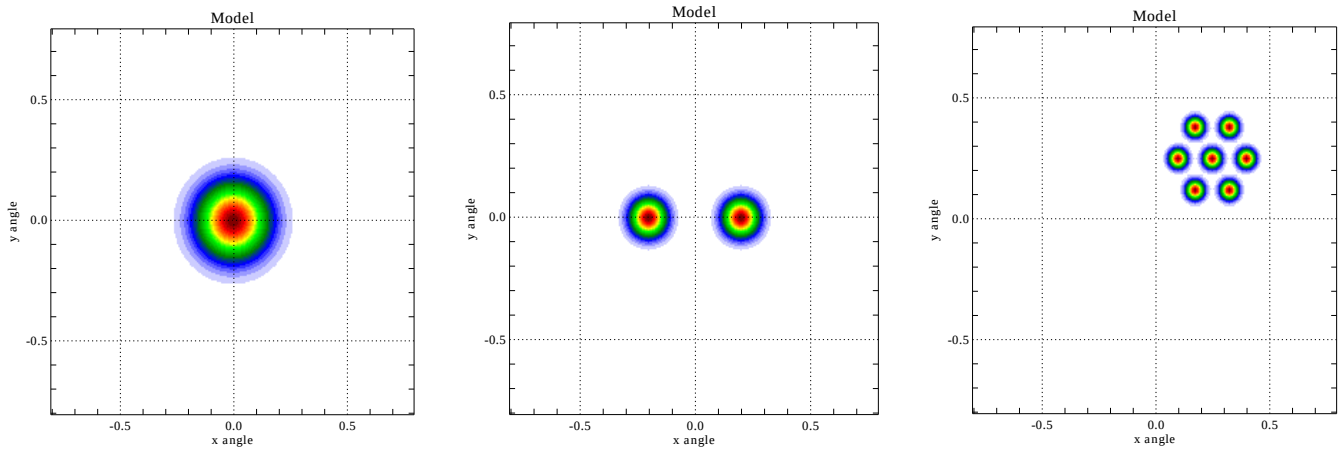

Fig. 1. The model brightnesses (true images) used as inputs to the simulations. The first model shows a single cylindrical structure. This is an (sort of baseline) image, as well as a reasonable representation of a single filament of enhanced scattering or a meteor trail echo. The second model shows two immediately neighbouring structures, which has been suggested to occur for naturally enhanced ion-acoustic echoes. The third model shows a tightly clustered group of very narrow structures. This is a crude representation of a bunch of striations which might be expected in heating experiments.

The Maximum Entropy method, related to the spectral estimation method of the same name, takes a quite different approach. This method considers all possible images, and between all images that are consistent with the (incomplete and noisy) observations, it chooses the one which can be realised in the greatest number of ways, i.e. has the highest entropy.

Maximum Entropy has a number of desirable properties for this application: It does not introduce artifacts for which there is no support in the data, and it results in an image which is "maximally smooth" in some sense. On the other hand, it is computationally intensive.

The Capon algorithm, which can be considered an adaptive beam-steering method, is very fast and gives good results for a good signal-to-noise ratio, which makes it better suited for real-time applications. In the Capon method, obtaining the image reduces to inverting the sample covariance matrix.

3.4 Suitability for other applications

We have seen that we can realise a design which will be capable of detecting and imaging moderately strong naturally enhanced ion-acoustic echoes. Next, we will see how this design is expected to perform for the other applications mentioned above.

3.4.1 HF-enhanced echoes

Using HF (heating), ionospheric plasma instabilities can be triggered artificially, which results in scattering levels much higher than thermal levels. For instance, Rietveld et al. (2002) sees an SNR of (24 dB) for 933 MHz, and (57 dB) for 224 MHz, and we can reasonably expect to observe something between these two levels with the ESR. The planned

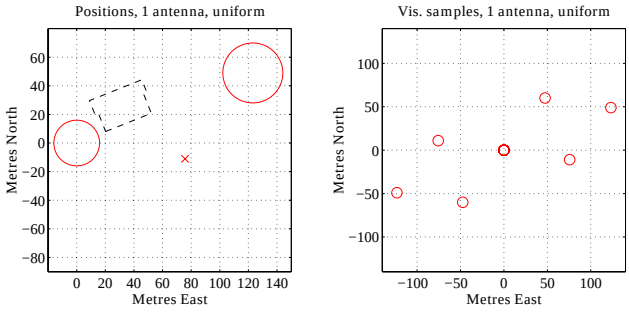

Fig. 2. The left panel shows the antenna configuration which will be used for the first passive receiving antenna, indicated by a cross. The antenna is placed in the centre of an equilateral triangle where the larger antennas, marked by circles of the diameter of each dish, form two of the three vertices. The position and orientation of the ESR building is indicated by the dashed outline. The panel to the right shows which points of the visibility function are sampled by this setup. As there are no short baselines in this configuration, the problems with aliasing rules out imaging, as the examples in Fig. 3 show. Even so, it will verify that it is possible to detect the signal in such an antenna, and that it is possible to estimate correlations between the signals in the large and the small antennas.

passive antennas should have no trouble observing a signal at these levels. Another question is whether the magnetic field and HF ray geometry on Svalbard will lead to the striations and their bunching observed at Arecibo. This can only be decided through observations.

3.4.2 PMSE

Although PMSE has been observed with the ESR, the scattering levels observed so far have been much lower than those

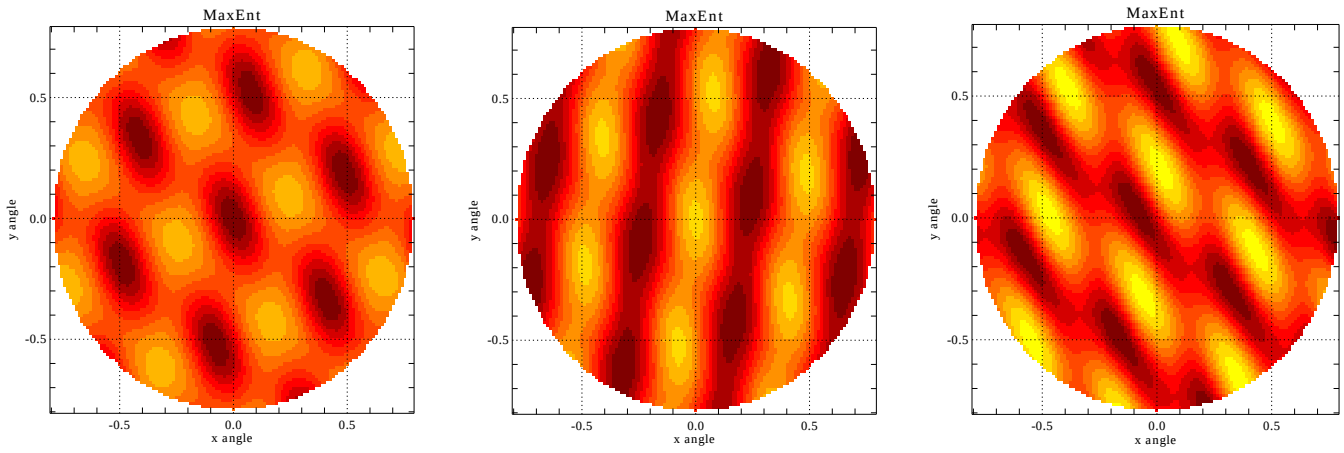

Fig. 3. Images obtained of the model brightnesses of Fig. 1 using the antenna configuration shown in Fig. 2 and a Maximum Entropy image inversion algorithm. Due to the lack of short baselines, the problems with aliasing are quite severe, and imaging is not possible. This configuration is still useful as a demonstration of the feasibility of obtaining useful signal and correlations out of the smaller antenna.

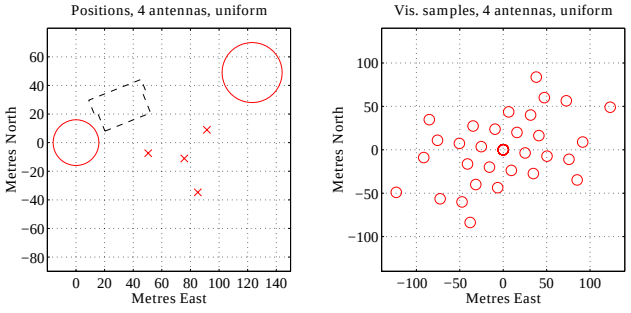

Fig. 4. A configuration for four passive receiving antennas, in the same format as Fig. 2. In this case, one antenna is placed at the centre of an equilateral triangle with the two existing antennas at two of the vertices, as before, and three passive antennas form another equilateral triangle concentric with the outer triangle, with side length one-third of the large triangle. The images obtained using this setup are shown in Fig. 5.

observed at VHF and lower frequencies, somewhere between 3 and 6 dB. At these power levels, it will be difficult to obtain a meaningful signal from the passive antennas currently being considered. It is also uncertain whether the scattering structures in PMSE are of a size which can be detected in the current configuration. The structures imaged at or near 50 MHz are wider than the ESR beam, but the coordinated SOUSY and ESR observations reported by Röttger (2001) show that the layer contributing to PMSE at ESR frequencies is much thinner (vertically) than that at 50 MHz. If a similar limiting factor works in the horizontal direction, such structures could be observable with the described setup.

3.4.3 Meteors

Meteor head echoes are the extremely short-lived and very localized echoes from the overdense plasma formed during the ablation of a meteoroid in the atmosphere (Wannberg et al., 1996). There are no reports of meteor observations with the ESR, but the SNR reported by Erickson et al. (2001) at 440 MHz leads us to expect a significant number of meteors observable with the ESR. The Millstone Hill observations were taken with an antenna of 45 dB gain and 1–2 MW transmitter power, but a higher system temperature than that of the ESR. The SNR seen with the ESR should not differ much from these reports, and the passive array should be capable of observing them. As these echoes arise from extremely localized regions, they are also an excellent target for imaging.

Meteor trail echoes have also been seen, and producing excellent SNR at UHF frequencies (Pellinen-Wannberg and Wannberg, 1994). These are also localized targets, which should work well for interferometry. The meteor trail orientation can then be used to compute the radiant point, as demonstrated by Chau and Woodman (2004).

4 Simulation results

To give an impression of the kind of images which can be obtained, we have generated several example brightness distributions comprising several Gaussian blobs. These have been Fourier transformed into a true visibility function. Using different imaginable antenna configurations including the existing ESR antennas and between one and five passive antennas, we have sampled this visibility function in a small number of points, defined by the baselines between antenna pairs. These visibility samples are then the input to the image inversion algorithms.

In the simulations, the pattern of the transmit antenna is represented by a sinc function corresponding to the 32 m diameter of the smaller of the existing antennas. The sinc pattern models the sidelobe pattern of the transmit antenna,

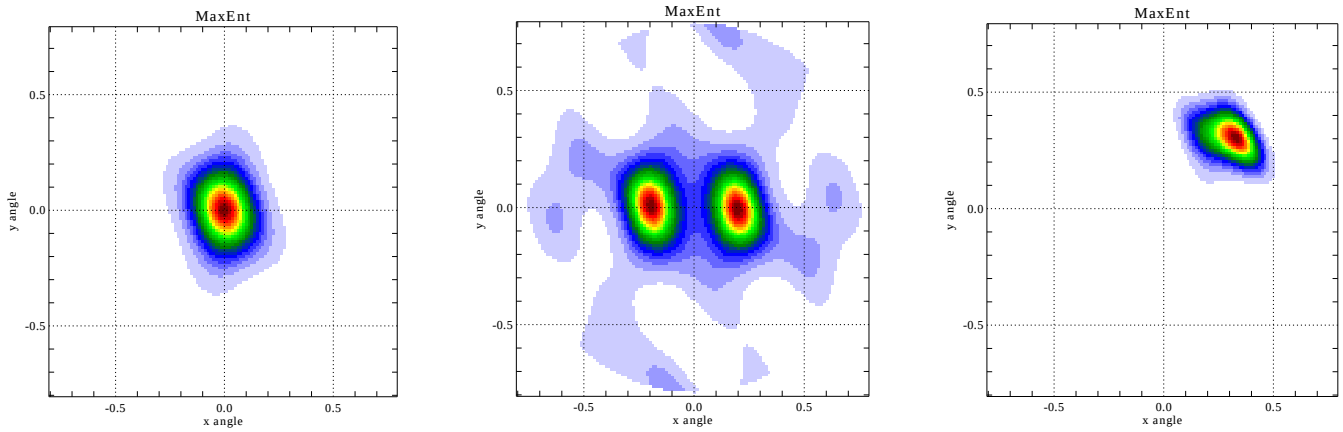

Fig. 5. Images of the model brightnesses of Fig. 1 obtained using the antenna configuration of Fig. 4 and the Maximum Entropy method.

although for the purposes of these simulations this does not matter much, as the model images have all been placed in the main beam. The receive antennas are represented by wider Gaussian patterns. The exact shape of the receive antenna pattern for the purpose of these simulations is less important, since the illumination of the scatterers is determined entirely by the transmitting antenna.

The different model brightnesses are shown in Fig. 1. The first model brightness is a single cylindrical structure with half-power width of 0.1° centered in the beam. This model is useful as a sort of "baseline" image, as it is very simple to see distortions and artifacts. At the same time, this is the image one would expect from a single filament of naturally enhanced ion-acoustic scattering, as well as a useful representation of a developed meteor trail echo for a meteor which has travelled directly towards the radar. (For meteor head echoes, an image which is point-like or a thin line should be used instead.)

The second model shows two identical cylindrical structures side-by-side. If naturally enhanced ion-acoustic echoes were to arise in immediately neighbouring regions of upward and downward streaming currents, the imager must be able to resolve the two structures.

The third model shows a broad structure which contains a large number of very narrow scattering structures. This corresponds to the "bunching" of filaments, or striations, observed by rockets in heating experiments. In this case, the imaging radar is not expected to resolve the individual striations, but it should still be able to provide information on the shape and size of the bunch.

While radar imaging of PMSE has been demonstrated at VHF frequencies (around 50 MHz), we also know that the scattering is very different at this frequency and the 500 MHz of the ESR (Hall and Röttger, 2001), and there are no imaging results that we are aware of for intermediate frequencies. The VHF imaging results show fairly large regions of scattering, but the results of Röttger (2000) indicates that there might be a much smaller scattering region at UHF frequencies.

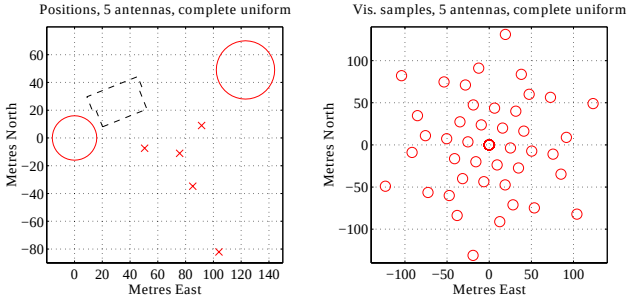

Fig. 6. A configuration for five passive receiving antennas, in the same format as Fig. 2. This is the same pattern as in Fig. 4, with an added receiving antenna at the third vertex of the outer triangle.

4.1 Antenna configurations

Antenna configurations are necessarily constrained by the location of the two existing antennas. Radio astronomy has decades of research on the optimal configurations under varying assumptions for the brightness distribution (e.g. Holdaway and Helfer, 1999). In our case, we want to make as few assumptions as possible regarding brightness, so we want to obtain a visibility sampling which is dense and close to uniform for short baselines, with few additional antennas and no redundant baselines. One way to achieve this is to have concentric, sucessively larger equilateral triangles with receiving antennas at the centre and vertices of each triangle. In the configurations suggested here, we have tried to approximate this pattern.

The initial deployment, scheduled for the summer and early fall of 2004, will position a single passive antenna in the centre of the equilateral triangle with the existing antennas in two of the three vertices. This configuration is sketched in Fig. 2. Since no short baselines are obtained in this setup, spatial aliasing cannot be eliminated, and imaging is not possible from this initial deployment, as can be seen from the examples in Fig. 3. The initial deployment is still useful, since it will demonstrate that useful signal levels can be

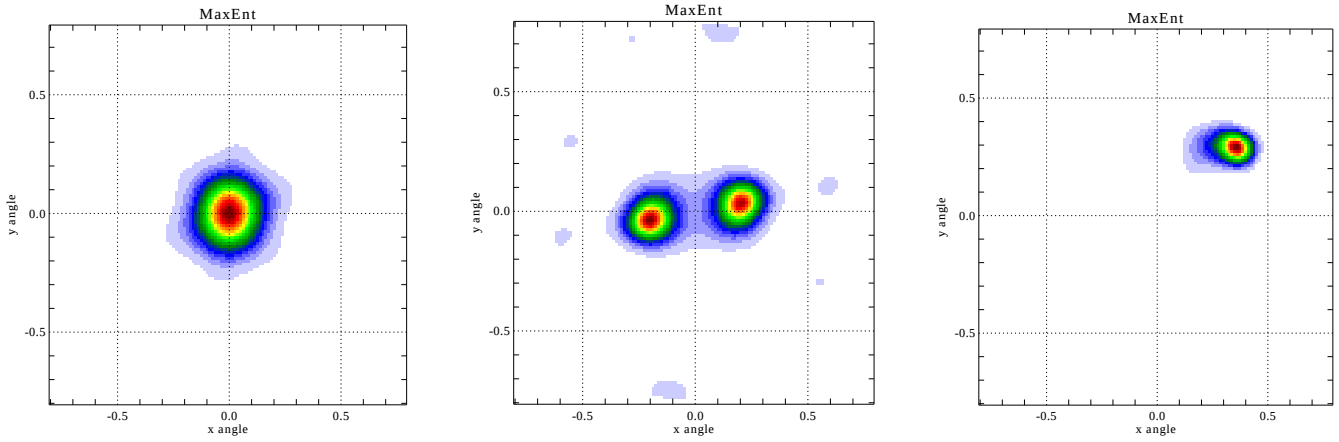

Fig. 7. Images of the model brightnesses of Fig. 1 obtained using the antenna configuration of Fig. 6 and the Maximum Entropy method. The slight tendency to elongate the features in the image seen in Fig. 5 is now gone.

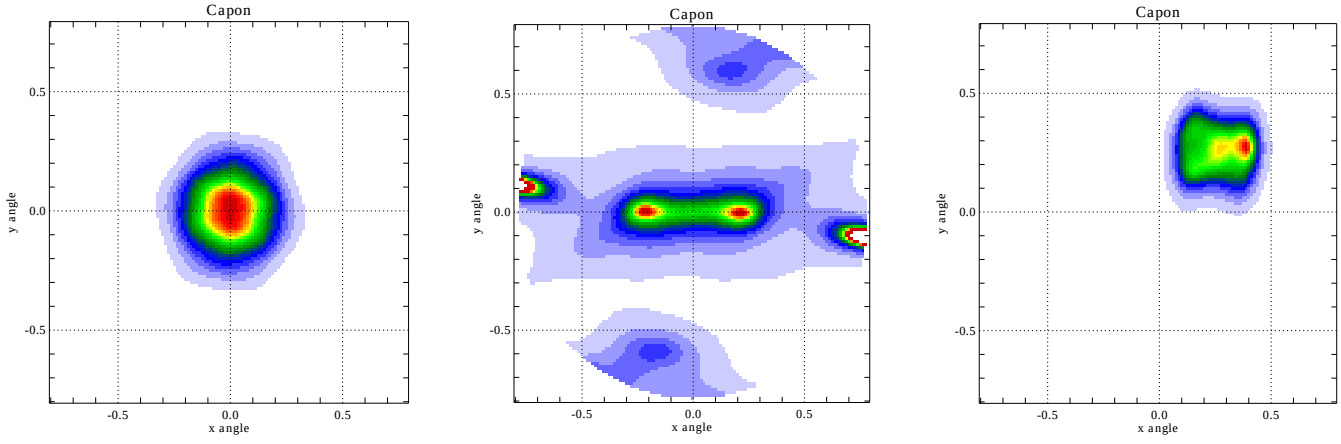

Fig. 8. Images of the model brightnesses of Fig. 1 obtained using the antenna configuration of Fig. 6 and the Capon method.

obtained using such small antennas, and that correlations between the signals in the smaller and larger antennas can be found.

A more promising configuration results when four passive antennas are used. In this case, short baselines are obtained between passive antennas, while the larger antennas form the vertices of the outer equilateral triangle. This configuration is shown in Fig. 4. In this configuration, the inner part of the visibility function is relatively densely sampled, which eliminates the spatial ambiguity, as can be seen in the simulated images in Fig. 5. The outer triangle does not have an antenna in the third vertex, which means that the longest baselines in the NW-SE direction are missing, resulting in some elongation in this direction in the inverted images. It is also interesting to note that while the method seems to give a reasonable impression of the size of the single and dual scatterers in the first two images, the size of the group of scatterers in the third image appears to be underestimated.

A fifth passive antenna can be used to occupy the final vertex of the outer triangle which completes the seven-antenna configuration. The visibility function is now sampled in a symmetric pattern, so full two-dimensional images can be obtained without preferred directions. In the first two images, this is observed as symmetric-looking patterns. The size of the group of scatterers in the third image is still underestimated. Of course, the large collecting area of the existing antennas might still mean that any baselines involving one or both of these is likely to achieve more significant correlations, particularly in marginal signal-to-noise situations.

As mentioned above, the Capon method can be valuable, particularly for real-time monitoring purposes. The method performs particularly well with high signal levels. Figure 8 shows examples of images obtained using the full seven-antenna configuration of Fig. 6 and the Capon method. We see that the method provides good estimates of the size and position of the scatterer in the first case; that it correctly positions the two scatterers in the second image, although it has

some problems with alias images at the edge of the field; and that it gives a better representation of the size of the group of scatterers in the third case than that given by the maximum entropy method.

5 Summary

We have presented our plan for adding an imaging interferometric capability to the EISCAT Svalbard Radar by means of a small number of passive receiver antenna arrays in conjuction with the existing facilities. There are a number of highly interesting studies being conducted at high latitudes focusing on ever smaller structures, including observations of naturally (and, in the near future, artificially) enhanced ion-acoustic echoes, PMSE and meteors. An imaging capability will therefore immediately have a number of applications, and it can contribute to the studies of many regions of the near-Earth space environment.

Using commercially available, off-the-shelf products where available (e.g. TV antennas), existing designs (reusing EISCAT's design for the analog receiver), and readily available software (from the MIDAS-W Software Radar prototype), we expect that the cost of such a project can be kept low. As there are no transmitters in the system, power demands are negligible and there are no added safety or licensing issues to speak of. Our choice for antenna technology means a very limited environmental impact, and permission to construct the antennas has already been obtained. The low cost and modest size and modularity of the antennas themselves means that any damage from severe weather can easily be replaced or repaired. Entire arrays can be moved quickly and painlessly should EISCAT decide to expand the ESR to more antennas. In short, we assess the construction of such a facility to be a realistic project, and an undertaking well worth the effort involved.

Acknowledgements. T. Grydeland, C. La Hoz and A. Brekke have been supported through grants 153358/431 "EISCAT/ESR related studies" and 159524/V30, "The polar upper atmosphere and beyond" from the NFR of Norway.

The authors wish to thank EISCAT Scientific Association assistant director G. Wannberg and R. Larsen of for their valuable observations and insights regarding choices for receiver and antenna technologies; and director T. van Eyken for valuable comments and suggestions for the manuscript. We would also like to thank EISCAT for agreeing to provide the necessary space for storage and equipment relevant to this project.

Topical Editor M. Lester thanks I. McCrea and another referee for their help in evaluating this paper.

References

Ables, J. G.: Maximum entropy spectral analysis, Astron. Astrophys. Suppl., 15, 383–393, 1974.

Blixt, E. M., Grydeland, T., Ivchenko, N., Hagfors, T., La Hoz, C., Lanchester, B. S., Løvhaug, U. P., and Trondsen, T. S.: Dynamic rayed aurora and enhanced ion-acoustic radar echoes, Ann. Geophys., 23, 3–11, 2005.

Briggs, D. S., Schwab, F. R., and Sramek, R. A.: Imaging, in: Synthesis Imaging in Radio Astronomy II, edited by: Taylor, G. B., Carilli, C. L., and Perley, R. A., chap. 7, 127–149, 1999.

Capon, J.: High-resolution frequency-wavenumber spectrum analysis, Proc. IEEE, 57, 1408–1419, 1969.

Chau, J. L. and Woodman, R. F.: Three-dimensional coherent radar imaging at Jicamarca: comparison of different inversion techniques, J. Atmos. Sol. Terr. Phys., 63, 253–261, doi:10.1016/S1364-6826(00)00142-5, 2001.

Chau, J. L. and Woodman, R. F.: Observations of meteor-head echoes using the Jicamarca 50 MHz radar in interferometer mode, Atmos. Chem. Phys., 4, 511–521, 2004, **SRef-ID: 1680-7324/acp/2004-4-511**.

Cho, J. Y. N. and Röttger, J.: An updated review of polar mesosphere summer echoes: Observation, theory, and their relationship to noctilucent clouds and subvisible aerosols, J. Geophys. Res., 102, 2001–2020, doi:10.1029/96JD02030, 1997.

Close, S., Hunt, S. M., McKeen, F. M., and Minardi, M. J.: Characterization of Leonid meteor head echo data collected using the VHF-UHF Advanced Research Projects Agency Long-Range Tracking and Instrumentation Radar (ALTAIR), Radio Sci., 37, 1009, doi:10.1029/2000RS002602, 2002.

Collis, P. N., Häggström, I., Kaila, K., and Rietveld, M. T.: EISCAT radar observations of enhanced incoherent scatter spectra; their relation to red aurora and field-aligned currents, Geophys. Res. Lett., 18, 1031–1034, 1991.

Erickson, P. J., Lind, F. D., Wendelken, S. M., and Faubert, M. A.: Meteor head echo observations using the Millstone Hill UHF incoherent scatter radar system, Proc. of Meteoroids 2001 Conference, Swedish Institute of Space Physics Kiruna, Sweden, 457–463, 2001.

Farley, D. T., Ierkic, H. M., and Fejer, B. G.: Radar interferometry: A new technique for studying plasma turbulence in the ionosphere, J. Geophys. Res., 86, 1467–1472, 1981.

Grydeland, T., La Hoz, C., Hagfors, T., Blixt, E. M., Saito, S., Strømme, A., and Brekke, A.: Interferometric observations of filamentary structures associated with plasma instability in the auroral ionosphere, Geophys. Res. Lett., 30, 1338, doi:10.1029/2002GL016362, 2003.

Grydeland, T., Blixt, E. M., Løvhaug, U. P., Hagfors, T., La Hoz, C., and Trondsen, T. S.: Interferometric radar observations of filamented structures due to plasma instabilities and their relation to dynamic auroral rays, Ann. Geophys., 22, 1115–1132, 2004, **SRef-ID: 1432-0576/ag/2004-22-1115**.

Grydeland, T., Lind, F. D., Erickson, P. J., and Holt, J. M.: Software radar signal processing, Ann. Geophys., 23, 109–121, 2005.

Hall, C. M. and Röttger, J.: Initial observations of Polar Mesosphere Summer Echoes using the EISCAT Svalbard Radar, Geophys. Res. Lett., 28, 131–134, doi:10.1029/2000GL003821, 2001.

Högbom, J. A.: Aperture synthesis with a non-regular distribution of interferometer baselines, Astron. Astrophys. Suppl., 15, 417–426, 1974.

Holdaway, M. A. and Helfer, T. T.: Interferometric array design, in: Synthesis Imaging in Radio Astronomy II, edited by: Taylor, G. B., Carilli, C. L., and Perley, R. A., chap. 27, 537–563, 1999.

Holt, J. M., Erickson, P. J., Gorczyca, A. M., and Grydeland, T.: MIDAS-W: a workstation-based incoherent scatter radar data acquisition system, Ann. Geophys., 18, 1231–1241, 2000, **SRef-ID: 1432-0576/ag/2000-18-1231**.

Hysell, D. L.: Radar imaging of equatorial *F* region irregularities with maximum entropy interferometry, Radio Sci., 31, 1567–1578, doi:10.1029/96RS02334, 1996.

Hysell, D. L.: Imaging coherent backscatter radar studies of equatorial spread *F*, J. Atmos. Sol. Terr. Phys., 61, 701–716, doi:10.1016/S1364-6826(99)00020-6, 1999.

Isham, B., Rietveld, M. T., Hagfors, T., La Hoz, C., Mishin, E., Kofman, W., Leyser, T. B., and van Eyken, A. P.: Aspect angle dependence of HF enhanced incoherent backscatter, Adv. Space Res., 24, 1003–1006, doi:10.1016/S0273-1177(99)00555-4, 1999.

Janches, D., Pellinen-Wannberg, A., Wannberg, G., Westman, A., Häggström, I., and Meisel, D. D.: Tristatic observations of meteors using the 930 MHz European Incoherent Scatter radar system, J. Geophys. Res., 107, doi:10.1029/2001JA009205, 2002.

Jaynes, E. T.: On the rationale of maximum-entropy methods, Proc. IEEE, 70, 939–952, 1982.

Kelley, M. C., Arce, T. L., Salowey, J., Sulzer, M., Armstrong, W. T., Carter, M., and Duncan, L.: Density depletions at the 10-m scale induced by the Arecibo heater, J. Geophys. Res., 100, 17 367–17 376, doi:10.1029/95JA00063, 1995.

Kosch, M. J., Rietveld, M. T., Hagfors, T., and Leyser, T. B.: High-latitude HF-induced airglow displaced equatorwards of the pump beam, Geophys. Res. Lett., 27, 2817–2820, doi:10.1029/2000GL003754, 2000.

Kudeki, E. and Sürücü, F.: Radar interferometric imaging of field-aligned plasma irregularities in the equatorial electrojet, Geophys. Res. Lett., 18, 41–44, 1991.

Lind, F. D., Grydeland, T., Erickson, P. J., and Holt, J. M.: The Open Radar Initiative: Reliable technology for radio science, Radio Science Bulletin, 48–50, 2003.

Pellinen-Wannberg, A. and Wannberg, G.: Meteor observations with the EISCAT UHF incoherent scatter radar, J. Geophys. Res., 99, 11 379–11 390, doi:10.1029/94JA00274, 1994.

Rietveld, M. T., Isham, B., Grydeland, T., La Hoz, C., Leyser, T. B., Honary, F., Ueda, H., Kosch, M., and Hagfors, T.: HF-pump-induced parametric instabilities in the auroral E-region, Adv. Space Res., 29, 1363–1368, doi:10.1016/S0273-1177(02)00186-2, 2002.

Rietveld, M. T., Kosch, M. J., Blagoveshchenskaya, N. F., Kornienko, V. A., Leyser, T. B., and Yeoman, T. K.: Ionospheric electron heating, optical emissions, and striations induced by powerful HF radio waves at high latitudes: Aspect angle dependence, J. Geophys. Res., 108, 1141, doi:10.1029/2002JA009543, 2003.

Röttger, J.: Radar investigation of the mesosphere, stratosphere and the troposphere in Svalbard, Adv. Polar Upper Atmos. Res., 14, 202–220, 2000.

Röttger, J.: Observations of the polar *D*-region and the mesosphere with the EISCAT Svalbard Radar and the SOUSY Svalbard Radar, Mem. Natl Inst. Polar Res., Spec. Issue, 54, 9–20, 2001.

Röttger, J. and Ierkic, H. M.: Postset beam steering and interferometer applications of VHF radars to study winds, waves, and turbulence in the lower and middle atmosphere, Radio Sci., 20, 1461–1480, 1985.

Sedgemore-Schulthess, K. J. F., Lockwood, M., Trondsen, T. S., Lanchester, B. S., Rees, M. H., Lorentzen, D. A., and Moen, J.: Coherent EISCAT Svalbard Radar spectra from the dayside cusp/cleft and their implication for transient field-aligned currents, J. Geophys. Res., 104, 24 613–24 624, doi:10.1029/1999JA900276, 1999.

Sulzer, M. P.: Meteoroid velocity distribution derived from head echo data collected at Arecibo during regular world day observations, Atmos. Chem. Phys., 4, 947–954, 2004,
SRef-ID: 1680-7324/acp/2004-4-947.

Taylor, G. B., Carilli, C. L., and Perley, R. A. (Eds.): Synthesis Imaging in Radio Astronomy II, in: Astronomical Society of the Pacific Conference Series, vol. 180, Astronomical Society of the Pacific, San Francisco, CA, ISBN 1-58381-005-6, 1999.

Wannberg, G., Pellinen-Wannberg, A., and Westman, A.: An ambiguity-function-based method for analysis of Doppler decompressed radar signals applied to EISCAT measurements of oblique UHF-VHF meteor echoes, Radio Sci., 31, 497–518, doi:10.1029/96RS00088, 1996.

Wannberg, G., Wolf, I., Vanhainen, L.-G., Koskenniemi, K., Röttger, J., Postila, M., Markkanen, J., Jacobsen, R., Stenberg, A., Larsen, R., Eliassen, S., Heck, S., and Huuskonen, A.: The EISCAT Svalbard radar: a case study in modern incoherent scatter radar system design, Radio Sci., 32, 2283–2307, doi:10.1029/97RS01803, 1997.

Wilczek, R. and Drapatz, S.: A high accuracy algorithm for maximum entropy image restoration in the case of small data sets, Astron. Astrophys., 142, 9–12, 1985.

Woodman, R. F.: Inclination of the geomagnetic field measured by an incoherent scatter technique, J. Geophys. Res., 76, 178–184, 1971.

Woodman, R. F.: Coherent radar imaging: Signal processing and statistical properties, Radio Sci., 32, 2373–2391, doi:10.1029/97RS02017, 1997.

Wright, D. M., Davies, J. A., Robinson, T. R., Chapman, P. J., Yeoman, T. K., Thomas, E. C., Lester, M., Cowley, S. W. H., Stocker, A. J., Horne, R. B., and Honary, F.: Space Plasma Exploration by Active Radar (SPEAR): an overview of a future radar facility, Ann. Geophys., 18, 1248–1255, 2000,
SRef-ID: 1432-0576/ag/2000-18-1248.

Yu, T.-Y., Palmer, R. D., and Chilson, P. B.: An investigation of scattering mechanisms and dynamics in PMSE using coherent radar imaging, J. Atmos. Sol. Terr. Phys., 63, 1797–1810, doi:10.1016/S1364-6826(01)00058-X, 2001.

Zhou, Q. H. and Kelley, M. C.: Meteor observations by the Arecibo 430 MHz incoherent scatter radar. II. Results from time-resolved observations, J. Atmos. Sol. Terr. Phys., 59, 739–752, doi:10.1016/S1364-6826(96)00103-4, 1997.